Influence of Radial Stiffness Gradients on Porous Composite Bulk Mechanics

Melissa R. Abed [†,1], *Erin S. Archibeck* [†,1], *Roger S. Isied* [†,1], *Yarah Feteih* [1], *Grace D. O'Connell* [1], *Grace X. Gu* [*,1]

[1]Department of Mechanical Engineering, University of California, Berkeley, USA

Keywords: *Functionally Gradient Materials, Finite Element Modeling, CT, 3D Printing, PolyJet Printing, Bioinspired Materials, Composites*

Functionally gradient materials, characterized by a smooth compositional change over space, have gained attention in recent years due to their tunable properties and ability to reduce mechanical stress concentrations. Specifically, attaining high stiffness without compromising toughness is a challenge, as the properties are inversely related. Varying moduli gradients, as seen abundantly in biological materials, do not present this trade-off, facilitating increased rigidity without altering maximum elongation. In this paper, the application of stiffness gradients in porous structures is investigated through compressive mechanical testing, computerized tomography imaging, and finite element modeling. Gradients are compared to several alternative designs to investigate the importance of a smooth material transition and increased radial stiffness. All groups are compressed to 50% strain and the pre- and post-pore closure modulus, toughness, and dimensional change in the transverse and radial directions are measured. The findings indicate that a mechanical gradient with increasing radial stiffness allows for balance of mechanical integrity and favorable recovery characteristics, crucial for long-lasting performance. Furthermore, the structures with an increasing radial stiffness out-perform those with a decreasing radial stiffness in all aspects. The results emphasize the mechanical advantages and optimization potential of a radial stiffness gradient for a wide range of load-bearing applications.

1   Introduction

Mechanical gradients are commonly observed in materials throughout the body and in nature. For example, mechanical performance of bones [1], teeth [2], tendon-to-bone insertion sites [3], and arteries [4] are due to gradients in tissue composition and structure. A smooth progression in material properties offer many advantages, including the ability to simultaneously exhibit both high stiffness and toughness, properties that are often mutually exclusive [5]. Many load-bearing structures require heterogeneous material properties. However, materials with a blunt interface can induce undesirable stress concentrations and strain mismatches at the transition [6]. Mechanical gradients have the potential to overcome this obstacle, allowing for improved functionality and increased failure and recovery properties [7]. For this reason, gradients have been employed in a variety of industries, including aerospace, electronics, and biomedical implants [7].

The benefits of replicating structural and compositional gradients in biomedical applications are extensive. Utilizing multi-layered materials with a smooth compositional gradient in medical implants allow for better recapitulation of spatial variations in mechanical behavior of native tissues [8]. Pertinently, materials with compositional gradients have been shown to have better structural integrity and increased life compared to a homogeneous counterpart [9], an important factor for reducing the need for revision surgery. Maximum stress and overall energy absorption, which is important for supporting the continuous loads during daily activity, have also been shown to be greater in gradient structures [10]. For example, bone scaffolds are common biomedical implants that utilize both compositional and pore size gradients to mimic the native tissue [8].

The intervertebral disc (IVD) is the load bearing tissue of the spinal column. The disc must withstand complex six-degrees-of-freedom dynamic loading during daily activities. There has been growing interest in developing implantable materials that aim to replicate the function of the healthy IVD using three-dimensional (3D) printing techniques [11, 12]. Recently, 3D printing was used to create a porous scaffold for the IVD, where spaces between deposited material would allow cells to deposit extracellular ma-

---

[†]Equal first co-authorship.
[*]Corresponding author: ggu@berkeley.edu

trix [13]. While the scaffold incorporates a pattern density to attempt replication of the difference in strength throughout the disc, the design strategies in previous work do not focus on mechanical integrity and predictive failure. Mechanical integrity under compressive loading is a required obstacle that must be addressed before clinical application [12, 14, 15, 16] through the use of a compositional gradient. Most scaffolds have been created using a single material, which has been shown to create undesirable stress concentrations [6] and does not replicate gradients in stiffness and composition, which is important for stress distribution and mechanical function in healthy stable discs [17, 18].

Advances in additive manufacturing equipment allow for multiple materials to be used in a single print or design. This enables the use of compositional gradients in the design of biological tissue analogs. Specifically for the IVD, there are two primary regions with drastic differences in tissue structure, composition, and function. The disc is comprised of the soft gelatinous nucleus pulposus (NP), which is semi-constrained by the annulus fibrosus (AF), a fiber-reinforced composite with alternating layers of stiff collagen fiber sheets (Figure 1). Even within the AF, gradients in tissue composition and structure are observed from the inner AF to the outer AF, with the outer AF being stiffer [7]. Under mechanical loading, the NP absorbs most of the compressive load, ultimately applying radial tensile stresses to the AF. The outer AF acts to reduce overall disc bulging, while the more flexible and softer inner AF helps to absorb the stresses transferred from the NP [19]. While a mechanical gradient is crucial for biological load-bearing tissues such as the disc, there is limited research on application and mechanical properties of a stiffness material gradient in a porous structure. Porous structures are crucial for replicating biological tissue such as in an intervertebral scaffold design. Furthermore, while demonstrated in natural material, the importance of an increased radial stiffness with a smooth transition has never been measured. Therefore, it is critical to understand how increased radial stiffness and a smooth transition will influence modulus, recovery, and fracture.
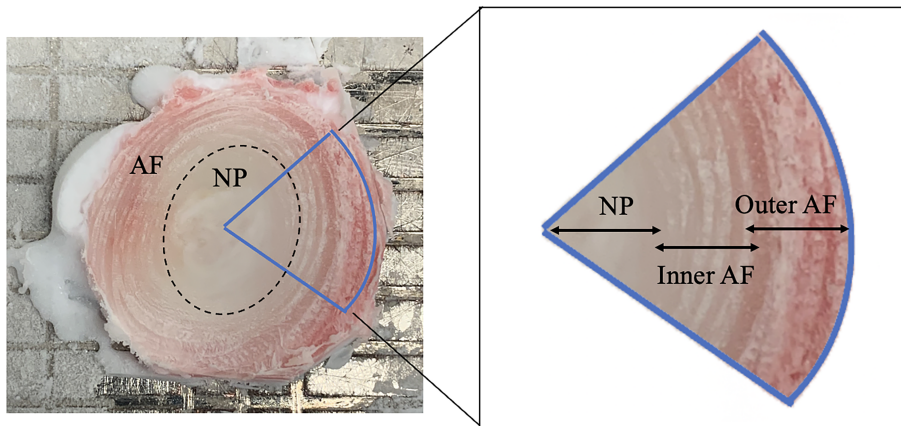

Figure 1: Dissected frozen bovine intervertebral disc. The compositional gradient through the NP, inner AF, and outer AF is depicted. The dashed oval encompasses the NP

.

The primary objective of this study was to highlight benefits of employing a bioinspired radially increased stiffness design on compressive mechanical behavior. To do so, the mechanical properties and failure behavior of a 3D printed porous mechanical gradient composite design were compared to its homogeneous counterparts. As the IVD naturally incorporates a radial stiffness gradient and undergoes compressive loading, the general geometry of a porous IVD scaffold was replicated [13]. The specific specimen geometry was selected as it has already been proven to provide adequate housing for cell culturing but has limited mechanical integrity, crucial for its load-bearing application. 3D printed scaffolds were fabricated and mechanically tested with several material designs to understand the importance of an increased radial stiffness gradient with respect to mechanical integrity of the bulk structure, fracture behavior, and recovery after loading. Particularly, a five-material gradient with an increase in stiffness from the center to the outside was compared under compressive loading to reverse gradient, two-material, and homogeneous materials.

While there is an abundance of research on replicating or replacing tissues through the use of scaffolds [12, 13, 15, 16, 20, 21, 22], there is a shortcoming of research on structural integrity. Specifically, the mechanical properties and recovery behavior of incorporating a material gradient with increased stiffness has never been studied. Radial stiffness gradients will play a principal structural role in developing future biological implants that undergo compressive loading, such as IVD and trabecular bone scaffolds. Additionally, gradients provide design parameters for fine-tuning of mechanical properties through material selection, gradient structure, and geometric optimization. Therefore, the increased radial stiffness gradient can also be applied to a wide range of structural applications, including the automotive, aerospace, and civil industries.

2 Methods

2.1 Design Considerations

A computer aided design of the geometry was created based on the IVD scaffold design described in Wu et. al. [13]. The scaffolds were scaled to fall within the typical range of a human IVD disc size, with a disc height of 9 mm and a diameter (anterior-posterior plane) of 40 mm [23]. The overall geometry better resembled the geometry of a bovine caudal disc rather than the kidney bean shape of human IVDs. When scaling the disc height and diameter of the Wu et. al. scaffold design to the size of a human IVD, the resulting scaffold support struts scaled proportionally to 1 mm in diameter. The cross-sectional view was split radially into five separate sections to tune for specific material gradients in the radial direction. This radial split along with the associated volume fractions of each layer are shown in Figure 2a. The initial split was at the center of the inner ring (split radially at 12.31 mm), depicting the steepest transition between the NP and the AF. After this initial transition, the remaining body is evenly split radially into 4 additional bodies (radial splits at 14.25 mm, 16.15 mm, and 18.10 mm, respectively). For the two-material specimens, the initial split created the inner and outer step of the specimen, where the two-material specimen consisted of the stiffest and most flexible materials.

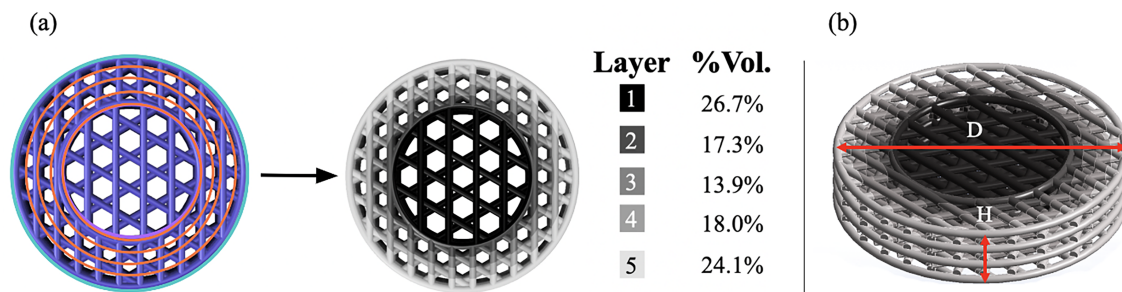| Layer	%Vol.
1	26.7%
2	17.3%
3	13.9%
4	18.0%
5	24.1%

Figure 2: Specimen material gradient splitting and overall geometry. (a) Material gradient body splitting. Pink lines illustrate radial split of five constituent materials. Layer 1 replicates the NP and layers 2-5 replicate the AF, with a stiffness gradient that increases toward layer 5.
(b) Profile of the specimen, with an initial height, H of 9 mm and an initial diameter, D of 40 mm.

2.2 3D Printing and Post-Processing

The specimens were fabricated with Stratasys Objet350 Connex3^{TM}, a multi-material PolyJet 3D printer. For the single material specimens, material assignment consisted of selecting the entire specimen body and assigning a single material. To assign materials to the gradient and two-material specimens, each radial section (Figure 2a) was selected individually and assigned to a separate material. Each specimen was removed from the print bed with a spatula. A low pressure water-jet was used to remove support material throughout the specimens. Removal was performed meticulously to avoid damage to the scaffolding.

2.3 Material Selection

The specimens were constructed using Stratasys digital materials which have been commonly used in previous literature [24, 25, 26, 27]. For the current iteration of the study, polymers were chosen that are not biocompatible. These polymers are used as a proxy in this work to study the effect of a mechanical gradient on the IVD scaffold design, but are not representative of real polymers that could feasibly be used in an IVD scaffold. The two base resins used were VeroPureWhite^{TM}, a rigid opaque photopolymer with mechanical properties most similar to acrylic, and TangoBlackPlus^{TM}, a thermoplastic elastomer with rubber-like characteristics. Additional materials, referred to as digital materials, were generated by blending different volume fractions of their proprietary polymer base resins, VeroPureWhite^{TM} and TangoBlackPlus^{TM}. These digital materials are preset mixtures available in Objet Studio, the software used to 3D print with Stratasys 3D printers and materials. To model the IVD, TangoBlackPlus^{TM} was used to mimic the flexible properties of the NP, while VeroPureWhite^{TM} was used to emulate the stiffer properties of the AF. FLX defines the softest, most rubbery material used in this study and is dark in color (Figure 3a), while RGD represents the class of the four stiffer materials utilized and is lighter in color (Figure 3b-e). The shade of gray of the digital materials is a visual indicator of the proportion of the FLX and RGD materials present. The numbers that follow FLX or RGD indicate the level of stiffness of the material; a larger number indicates a lower stiffness and a smaller number indicates a higher stiffness (e.g. RGD8530 is less stiff than RDG8515). FLX9895 was selected to mimic the NP's viscoelastic mechanical behavior, as FLX9895 also exhibits viscoelastic properties. Materials RGD8530, RGD8525, RGD8520, and RGD8515 were selected to mimic the AF due to the fibrous structure and composition of the AF which provide the tissue with high stiffness [28]. It should be noted that the AF becomes increasingly stiff from the inner radius of the IVD to the outer radius [29], which is why the materials were printed in the aforementioned order. While using a larger number of material steps in the gradient specimens would have been ideal to mimic the continuous natural gradient observed in the IVD, the number of materials used in this study were limited by the capabilities of Stratasys software and the desire to limit the size of the stiffness gradient between the innermost layer (Layer 1, Figure 2) and the outermost layer (Layer 5, Figure 2).

A two-material gradient consists of one transition between the softest and stiffest constituents moving radially outward from the specimen center. A gradient specimen is defined as five consecutive materials transitioning radially outward from the center of the specimen with increased stiffness. A reverse gradient (either two- or five-material) exemplifies a transition from the stiffest to the softest material, moving radially outward from the center of the specimen.

2.4 Mechanical Testing

Compression testing was performed with an Instron Model 5500 Series (Norwood, MA) equipped with compression platens. The fixtures are designed to evenly distribute compressive loading throughout the test specimen. The compression rate was 1 mm/min, in accordance with ASTM D695-02a [30]. Each specimen was compressed by half the average of the specimen heights —determined for each group type— measured prior to testing. At 50% compressive strain with respect to the initial specimen height, the test was concluded and the upper grip fixture was retracted for insertion of the subsequent specimen. Load-extension data was extracted from each run. To evaluate elastic recovery of the specimens, height and diameter measurements were taken at three different instances; prior to testing, immediately after testing, and 24 hours after testing.

2.5 Statistical Analysis

An unpaired t-test was performed to determine statistical significance between each measurement (modulus, toughness, change in diameter, change in height) for the four different multi-material groups against the single material RGD8530 group. A composite approach was used to select the RGD8530 group as the control through a weighted sum of the modulus of each constituent material. The weights were de-

fined by the associated volume fraction of each constituent. All multi-material groups had an approximated bulk modulus that was comparable to that of the RGD8530 group. Therefore, each measurement within every multi-material group was directly compared to that of the RGD8530 group. Data was reported as the average standard deviation, and statistical significance was assumed for p-values was less than or equal to 0.05.

2.6   Computed Tomography Scanning

Specimens were imaged using computed tomography (CT) to visualize internal damage accumulation (GE Healthcare eXplore Locus Micro CT scanner, 27 μm resolution). Two specimen groups (RGD8515 and gradient) were scanned before and 24 hours after compressive loading at 25% and 50% strain. A 4x4 bin mode was used to perform a two-frame stitching protocol to encompass the entire specimen surface area in the axial direction. The crop coordinates were reconfigured to ensure the specimen volume was encompassed within the image.

2.7   Finite Element Model

A finite element model of the specimens was created using Ansys Mechanical® Static Structural. The balance of linear momentum was solved to determine the deformation and equivalent stress on the specimen under specified loading and boundary conditions. The goal of this model was to approximate the aforementioned compression test in simulation to qualitatively gauge zones in which cracks are more likely to occur. A simple linear elastic constitutive model was used to observe the relative effects of strength between the different material types. The linear elastic properties used for each constituent material in the model was determined through tensile testing as described in 3.1.1 as well as [31]. The specimen CAD was imported directly into Ansys Workbench. An adaptive tetrahedron mesh refinement strategy was utilized using an average element size of 0.1 mm to ensure at least 10 elements spanned the diameter of each individual scaffold.

Two rigid surfaces were created as separate bodies above and below the specimen. A prescribed downward displacement was applied to the top surface while a fixed support boundary condition was applied to the bottom surface. For 25% deformed specimen simulations, the top plate was displaced by 2.25 mm, and for 50% deformed specimen simulations, the top plate was displaced by 4.5 mm. Both surfaces were assigned hardened steel material properties to act as a rigid material and ensure they would be minimally deformed while compressing the scaffold.

To apply the gradient material, the specimen CAD was radially split into five bodies. Bonded contacts were applied between different constitutive material sections in order to align boundary elements in each section such that the specimen was solved as a single body with varying spatial material parameters. A frictional contact constraint was placed between the specimen and both plates to allow for radial growth as it was compressed. Each body was assigned a material according to Figure 2a.

3   Results

3.1   Mechanical Testing

3.1.1   Specimen Fabrication

Nine specimen types were printed for mechanical testing, including five single-material specimens (Figure 3a-e), a two-material specimen (Figure 3f), a reverse two-material specimen (Figure 3g), a five-material reverse gradient specimen (Figure 3h), and a five-material gradient specimen (Figure 3i). Five specimens of each group were fabricated. The radial sections of the gradient specimen were assigned a material beginning from FLX for the inner radius and ending with RGD at the outermost radius, as shown in Figure 2a. Each of the five materials within the gradient specimen were used to create single material specimens. Tensile testing was performed for each material group using ASTM D638-14, Standard

Test Method for Tensile Properties of Plastics [32] at a rate of 5 mm/min to determine the elastic moduli values (Table 1). The elastic modulus was defined per ASTM D638-14 as the ratio of stress divided by strain in the linear region of the stress strain curve, where the stress was determined using the average original cross-sectional area of the gage length section of the specimen.
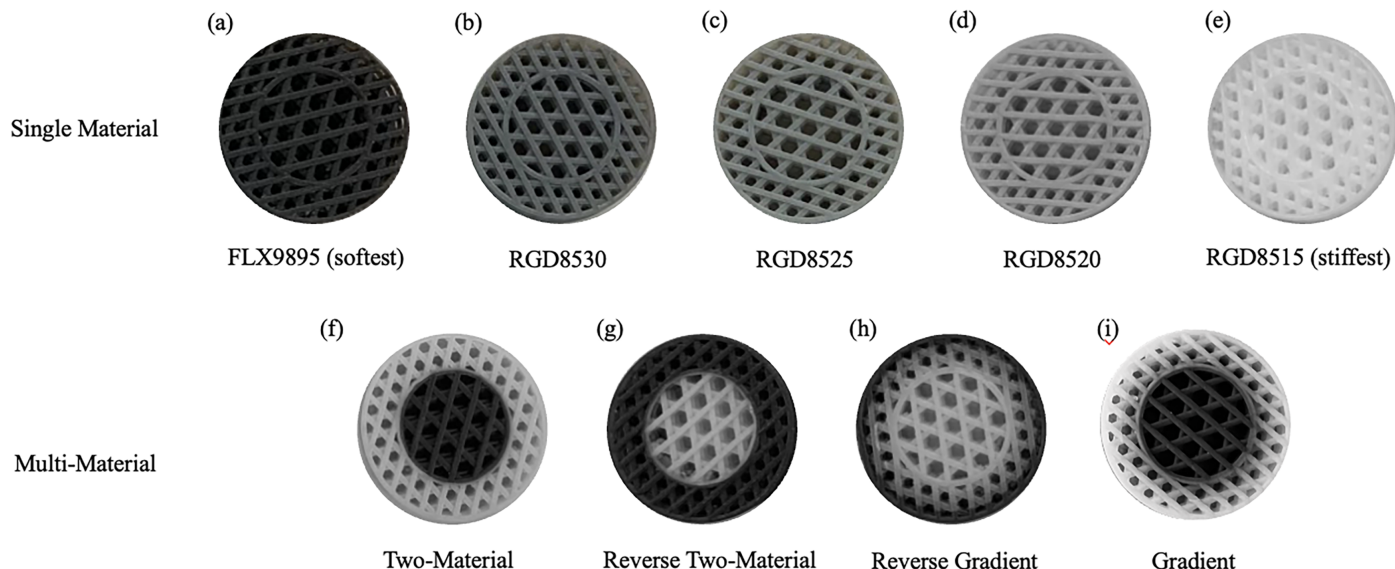

Figure 3: All 9 specimen types, single material specimens (a-e), two-material specimens (f, g), and five-material gradient specimens (h,i).

3.1.2   Stress-Strain Curve

An averaged stress-strain curve (Figure 4b) was generated by averaging each data point from the load-extension data for each specimen type shown (two-material, reverse two-material, reverse gradient, gradient). The stress was calculated using the load-extension data by dividing the applied load by the bulk cross-sectional area of the specimen. The bulk cross-sectional area was obtained from the CAD and does not account for the pores throughout the specimen.

This study defines toughness as the area under the stress strain curve up to 50% strain (yellow shading, Figure 4a). Toughness was calculated by integrating along the strain axis of the stress-strain curve using the composite trapezoidal rule.

Utilizing each individual stress-strain curve, the modulus of elasticity was measured as the slope of the linear portion of the curve [30], both pre- and post-pore closure (Figure 4a, red and purple lines, respectively). While the "linear" portion used for measuring the pre- and post-pore closure moduli is arbitrary, the curve-fit linear region was the same for each specimen. As the objective of this study was to compare different mechanical gradients, moduli were compared between the 9 specimen groups rather than compared to values in the literature for native tissues. Results for the pre- and post-pore closure moduli and toughness were averaged for each specimen type and compared in Figure 5.

Under compression, the stress shows three distinctive stages for all specimens (excluding FLX), including a pre-pore closure linear stage from 0.05-0.15 strain, a plateau "stiffening" stage from 0.15-0.23 strain, and a post-pore closure linear densification stage from 0.23-0.50 strain (Figure 4b). Bulk compressive stiffness of the two-material specimen was greater than the five-material gradient specimens (Figure 4c - green line versus blue line), while the reverse two-material displayed lower strength compared to the five-material gradient specimens (Figure 4c - orange line versus blue line). It was observed that the stiffness increased as a function of volume fraction of RGD8515, as expected.

This three-stage deformation pattern is exemplary in most highly-porous structures [33]. In the pre-pore

Table 1: Elastic moduli values of Stratasys digital materials utilized for specimens.

Layer	Material	Elastic Modulus [MPa]
1	FLX9895	5.26
2	RGD8530	142.48
3	RGD8525	236.67
4	RGD8520	256.70
5	RGD8515	268.56

closure stage, the specimens experience linear deformation until pore closure begins. At the plateau stage, the pores are compressed until they make contact with one another. Once the cell walls make contact, the densification stage begins, in which there is a more dramatic increase in stress required to cause further deformation. In this stage, a fully-dense material is being compressed, and the material provides the bulk of compression resistance.

Contrastingly, the stress-strain curve for the FLX material (Figure 4a) can be categorized into two regions, including a simultaneous pre-pore closure and densification stage and a post-pore closure stage. The increased flexibility of FLX leads to simultaneous elastic deformation and pore closure, yielding a linear region from 0.00-0.25 strain. A similar post-pore closure stage where there is a significant increase in stress due to the more fully dense material, as observed in the other specimen types, occurs from 0.25-0.50 strain.
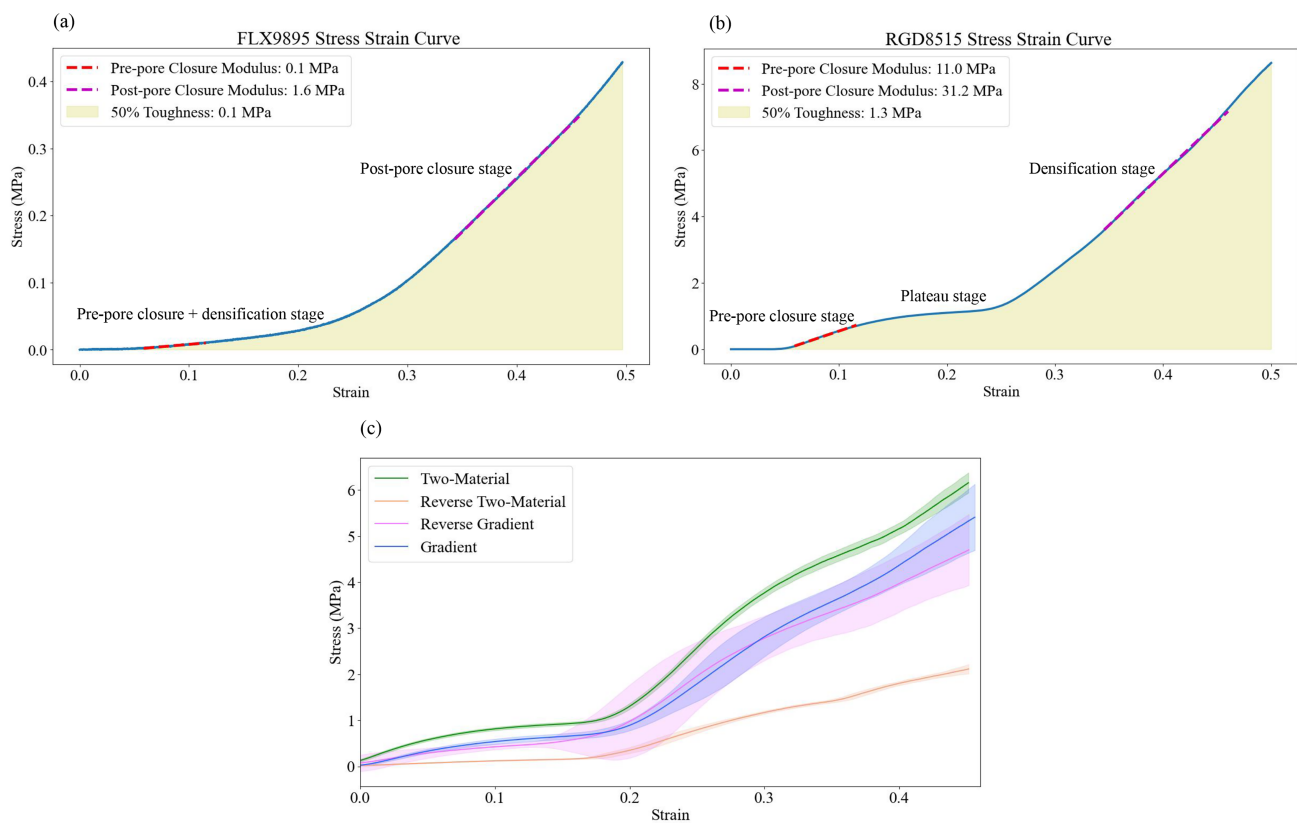

Figure 4: Compressive Stress-Strain Curves. (a) FLX9895 stress-strain curve highlighting toughness and pre-pore closure + densification and post-pore closure stages. (b) RGD8515 stress-strain curve highlighting toughness and pre-pore closure, plateau, and densification stages. (c) Averaged compressive stress-strain curve for the 4 multi-material specimen types and corresponding standard deviations (shaded regions).

3.1.3   Failure and Recovery

Overall specimen recovery was evaluated by examining dimensional recovery in both specimen height and diameter. Specimen height recovery was calculated as the percent change in height after loading

compared to the initial height prior to loading. Specimen diameter recovery was calculated as the percent change in diameter after loading compared to the initial diameter prior to loading.

Specimen height and diameter were measured immediately after loading to quantify the specimen's instantaneous recovery from 50% compressive strain. The samples were remeasured after 24 hours to quantify anelastic recovery and the total plastic deformation. Specimen height and diameter for all three time periods were averaged for each specimen group and the percent change with respect to the initial specimen height (Figure 5d) and diameter (Figure 5e) were calculated.

Both immediately and after 24 hours, the gradient specimens and the two-material specimens had a percent height change closer to the flexible material specimen, with the gradient specimens outperforming all specimen types except for FLX (Figure 5 d,e). These results indicate that the gradient specimen shows the greatest recovery potential, compared to single and two-material designs, which is crucial for performance under cyclic loading. The percent change in diameter was much smaller than that of the height (Figure 5 d,e). While the percent change in diameter was minimal, a similar trend was seen, where the RGD8515 material showed the largest percent change, while the gradient and two-material specimens showed the smallest percent changes both immediately after testing and after 24 hours.

Upon visual inspection of the specimens post-compression testing, the FLX specimens showed no visible sign of cracking, the RGD8515 specimens showed several signs of fracture and generally presented cracking across different cells, and the gradient and two-material specimens showed some cracking, with the majority seen at the material interfaces. These observations are further explored in Section 3.2.

3.1.4   Modulus and Toughness

In terms of pre- and post-pore closure modulus, the increased radial stiffness gradient specimens (both two- and five-material) outperformed all specimens except for the three stiffest single material specimens. This is despite the gradient specimens containing the smallest volume fraction of RGD amongst the specimen groups with the exception of the single material FLX specimen. All four multi-material specimens exhibited significantly higher toughness values than the single material specimens, with the two-material being the toughest, and the gradient being the second toughest.

3.2   Specimen Fracture: FE Model with CT validation

While quantitative experimental measurements provide an understanding of bulk properties, geometry dependent effects from loading are understood qualitatively through simulation and CT imaging. Four simulations were conducted according to the parameters in Section 2.7 comparing the RGD8515 and gradient specimen compressed to 25% and 50% strain. The simulation output the equivalent stress distribution over the specimen geometry. A section view of the specimen was observed on the second layer from the top of the specimen.

The maximum tensile stress values for each constituent were used as a baseline for comparison with other simulations. Figure 6 compares simulated equivalent stress distribution for these four specimens. Results shaded in red exceed the maximum tensile stress for each constituent as defined by Stratasys [31], and were considered as a potential failure region. The simulated results provided a qualitative understanding of where each specimen might fail.

Simulated results (Figure 6) depict the largest number of stress concentrations on the 50% compressed RGD8515 specimen. These stress regions are most prominent during the transition between the inner and outer ring where scaffolds are slightly offset from one another, restricting the outward radial load path. The gradient specimen displays lower stress concentrations between the inner and outer ring. In both cases, stress concentrations are observed at the outer ring of the specimens, consistent with both specimen types containing RGD8515 in their outermost regions. The 50% compressed RGD8515 specimen shows an onset of failure regions on the inner ring while the gradient specimen only shows the onset of failure regions in the outer ring where RGD8515 is placed.
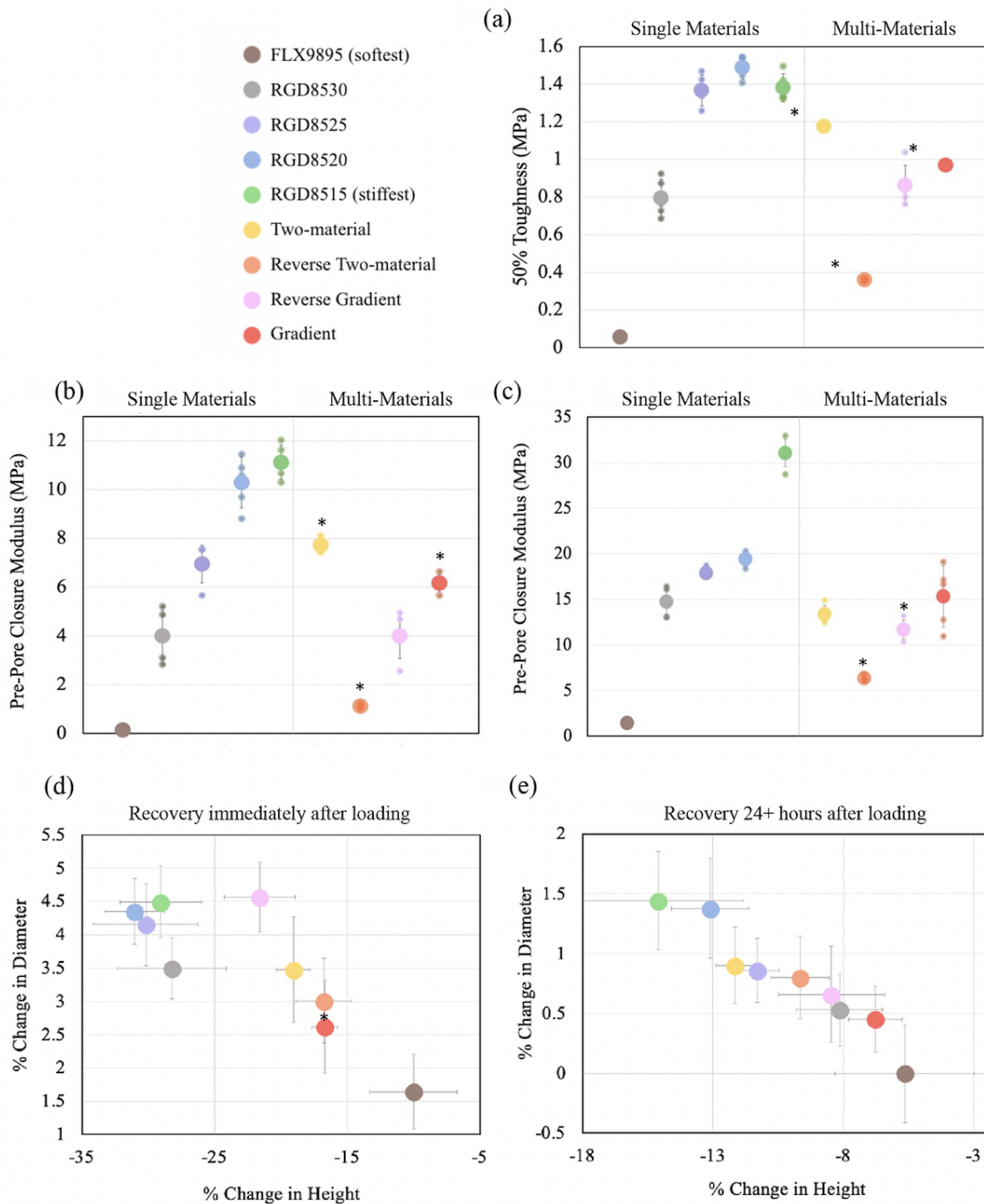
Figure 5: Mechanical and recovery properties of all nine specimen types. (a) 50% Toughness (MPa) (b) Pre-pore closure Modulus (MPa) (c) Post-pore closure Modulus (MPa) (d) Percent change in diameter versus percent change in height immediately after loading. The bottom right corner indicates most improved recovery. (e) Percent change in diameter versus percent change in height 24 hours after loading. The bottom right corner indicates most improved. * indicates statistical significance ($p < 0.05$) compared to the RGD8530 group.

CT images of the same four specimens described in Section 2.6 were collected. Figure 6 provides a direct visual comparison between the four specimens. Each CT scan was qualitatively inspected separately by three individuals for any failures from an axial vantage point. Failures were defined either as a *fracture* or *delamination*. A fracture was identified as a single discontinuity among the original geometry of the layer as illustrated on Figure 7. A delamination was identified as a separation of material at the same radial position in consecutive circumferential locations (Figure 7).
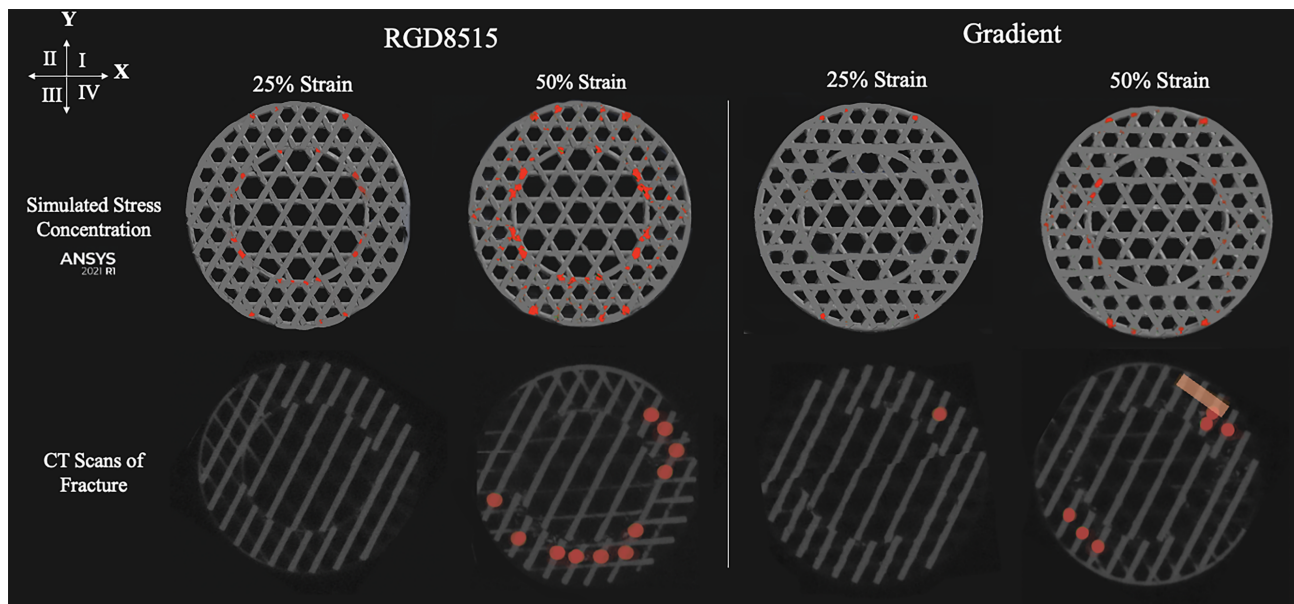
Figure 6: Simulated stress concentration (top) and CT scan outputs of the second specimen layer (bottom). Red circles denote fractured regions. Orange quadrilaterals denote delaminated regions.
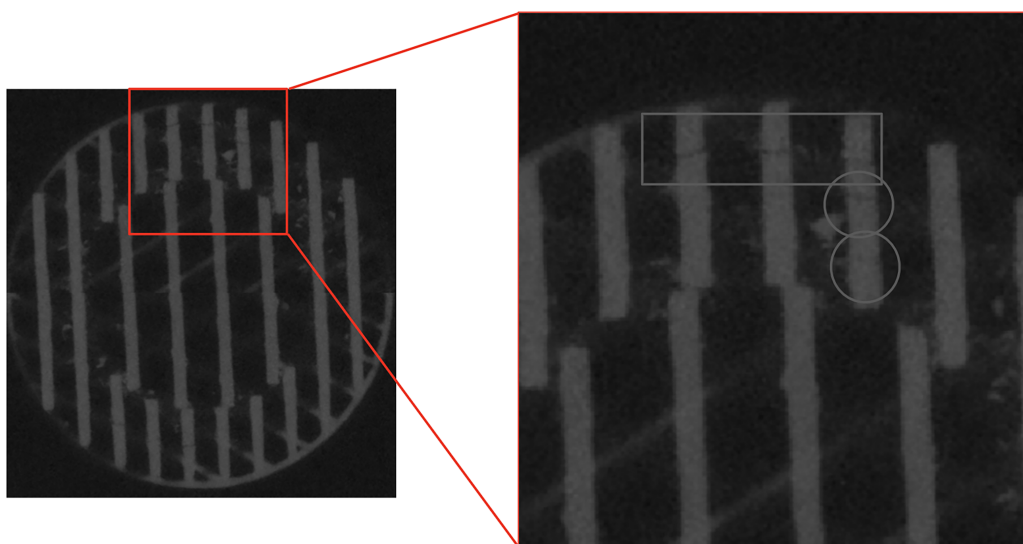

Figure 7: Layer 2 of an RGD8515 specimen at 50% strain. Circles denote a fracture location, while the rectangle denotes delamination.

Fracture was observed on the CT scans of the RGD8515 50% specimen in the same circumferential regions as that of the maximum stress regions of the simulated specimen. All simulations displayed stress concentrations on the positive and negative y-axis regions of the specimen on the outer ring where no fracture was observed on the CT images. Both the RGD8515 and gradient specimens show near fracture-free surfaces when compressed to 25% strain. The gradient specimen compressed to 25% strain exhibits a lone fracture near a material transition region.

When compressed to 50% strain, the gradient specimen shows significant improvement in the total number of observed fractures compared to its RGD8515 counterpart. The reduction in fractures can be seen particularly along the negative y-axis of the inner ring which is consistent with a reduction in maximum stress areas in the analogous simulated specimens. The fractures occurred in quadrants 1 and 3 of the x-y plane, consistent with stress concentration regions in the simulated specimen. The gradient specimen compressed to 25% strain did incur delamination at the material interface between RGD8515 and

RGD8520, the two stiffest of constituent materials. This can be potentially attributed to a reduced compliance in comparison to the other constituent materials. These delaminations can be minimized by utilizing an increased number of material steps and constituent materials to reduce the change in mechanical properties between each material step.

4 Discussion

4.1 Mechanical Testing

All comparisons of the gradient versus the reverse gradient in Figure 5 highlight the importance of increasing the stiffness gradient from the center to the edge of a cylindrical specimen. The stiffness gradient resulted in greater toughness, pre- and post-pore closure modulus, and recovery (diameter and height change) when compared to the gradient with a decreased radial stiffness. The performance of the increased stiffness gradient agrees with observations of native IVD mechanics [19, 34, 35], underlining the importance of a soft center to absorb the compressive load with a gradual stiffening towards the outer surface to reduce the radial tensile stresses. Additionally, the soft center alleviates stress concentrations through increased compliance, allowing for minimization of fracture and improved recovery [7].

Similarly, to study the importance of a smooth compositional progression, the gradient specimens are compared to the two-material specimens. While the two-material specimen type had a higher toughness and pre-pore closure modulus, this is due to its higher volume fraction of stiffer materials. The gradient exhibits a higher post-pore closure modulus and overall recovery immediately and 24+ hours after loading. Due to minimal stress concentrations in the gradient material (Figure 6) a smooth material transition improves overall recovery, crucial for all load-bearing applications [6, 7]. While this conclusion agrees with previous literature, compositional gradients have not been widely applied to improve the structural integrity of IVD scaffolds.

The increased radial stiffness gradient provides the best performance when considering toughness, elastic modulus, and recovery simultaneously. The RGD outperforms the gradient in toughness and elastic modulus but lacks in recovery. The FLX is superior in recovery but has very poor toughness and elastic modulus. As such, the gradient balances these 3 essential intrinsic properties essential to high performance of an IVD scaffold.

4.2 Specimen Fracture: FE Model with CT Validation

The FE model provides useful insight into specific regions of the specimen where higher stresses are expected which could be used to improve future scaffold designs. A simple constitutive model was chosen to observe relative effects of the same loading conditions on specimens with varying material properties. The results in Figure 6 demonstrate the efficacy of an increased radial stiffness gradient in comparison with a single constituent material specimen. While the locations of stress concentrations are geometry dependent and would be present regardless of the scaffold geometry chosen, the FE model results confirm that the material selection is the main driver of improvements between the single material and gradient specimens.

The CT images in Figure 6 demonstrate qualitative agreement with the simple FE model. The second layer from the top of the specimen was used for image and model comparison, as it was the layer with the largest number of fractures. Out of the 10 specimen layers, layers 2 and 9 presented the most fractures as well as the largest surface area of stress concentrations in the FE model which reduced moving towards the center of the specimen. Layers 1 and 10 presented no fractures. This can be attributed to the attachment of the outer layers to the flat metal chucks enforcing they maintain a flat surface. Layers 2 and 9 undergo the most compression due to loading conditions causing complex internal stresses. This leads to the large number of cracks developing at geometric interfaces between scaffolds.

5   Conclusion

An increased radial stiffness gradient, a solution inspired by biological tissue, offers a powerful and effective strategy to improve the overall mechanical performance of a compressive load-bearing application. The fabrication, mechanical testing, and analysis of porous composite structures helped deduce the following inferences: (1) an increased radial stiffness gradient outperforms a decreased radial stiffness gradient under compressive loading, (2) a smooth transition between stiffness outperforms a blunt transition between two heterogeneous materials, and (3) an increased radial stiffness captures an optimized balance of strength, toughness, and recovery compared to all other tested specimen types (single material, reverse two-material, and reverse gradient). First, an increased radial stiffness outperforms the reversed stiffness gradient under compression in all aspects. The increased radial gradient demonstrated larger modulus and toughness values, higher percent recovery, and decreased overall fracture. The center of the structure is softer, allowing for an absorption of the compressive stress while the outer rings become gradually stiffer, encompassing the tensile load on the structure. When reversed, the center is stiff and cannot absorb the load, leading to a dramatically decreased performance in every aspect, highlighting the importance of biomimicry. Furthermore, comparing the gradient structure to the two-material structure with a soft center, the gradient once again outperformed the two-material structure in all measurements. This is expected, as the smooth progression decreases stress concentrations throughout the structure.

There are several limitations in the present study that can be addressed in future work. The number of materials used was limited to 5 in order to minimize the radial stiffness gradient given the available material palette. Utilizing more materials with a controllable stiffness gradient matching that of the IVD can provide insight with regards to the quantitative effect of radial stiffness gradient on the strength and recovery of IVD scaffolds. This work can also be extended to include biocompatible polymers which can be fabricated using the same PolyJet process. However, mixing biocompatible materials to create a gradient requires additional manufacturing steps, which can negatively impact cell viability [36, 37, 38].

The conclusions made in this study regarding the superior performance of the gradient specimen were determined based on a comparison with the other created specimen types, but does not indicate that this specific gradient specimen is optimal for IVD scaffold design. A combinatorial optimization approach is required in the scope of increasing radial stiffness composites to determine an optimal constituent configuration for IVD loading and cell generation. The computational model is limited in terms of the material model available for the proprietary materials used in this study. A tensile test was conducted (section 2.4) to obtain linear elastic properties of each constituent which was used in the FE model to observe locations of high stress for comparison with CT scans of the specimens. An improved model would consider a nonlinear constitutive model to discern between elastic and plastic deformation of each specimen type. Obtaining this material model necessitates additional bending and flexural tests of each constituent material to accurately measure the associated nonlinear parameters.

From these results, two methods for improving a compressive load-bearing structure are possible: (1) a softer center with stiffer exterior (2) a smooth progression outward. Overall, a mechanical gradient with an increased radial stiffness provides an effective means to generate a structure with high strength, toughness, and recovery while minimizing overall fracture. Additionally, the location of fracture and compressive properties can be manipulated through material selection and gradient optimization. This can be utilized in a wide range of applications, such as developing IVD scaffolds. Future work will use the data from this study to develop a machine learning approach to optimize the mechanical gradient, including the number of material steps and material stiffness used in each step to achieve superior mechanical properties (e.g., strength, toughness, or recovery).

Declaration of Competing Interest

Acknowledgements

References

[1] M. Pope, J. Outwater, *Journal of Biomechanics* **1974**, *7*, 1 61.

[2] K. Bai, T. Zhang, Z. Yang, F. Song, X. Yang, K. Wang, *Chinese Science Bulletin* **2007**, *52*, 17 2310.

[3] J. Qu, A. R. Thoreson, Q. Chen, K.-N. An, P. C. Amadio, C. Zhao, *Journal of orthopaedic research* **2013**, *31*, 11 1713.

[4] G. D. Giannoglou, J. V. Soulis, T. M. Farmakis, G. A. Giannakoulas, G. E. Parcharidis, G. E. Louridas, *Medical engineering & physics* **2005**, *27*, 6 455.

[5] J. Mueller, J. R. Raney, K. Shea, J. A. Lewis, *Advanced Materials* **2018**, *30*, 12 1705001.

[6] K. Migacz, J. Chłopek, A. Morawska-Chochół, *Acta of Bioengineering and Biomechanics* **2014**, *16*, 3.

[7] D. Kokkinis, F. Bouville, A. R. Studart, *Advanced Materials* **2018**, *30*, 19 1705808.

[8] L. Diaz-Gomez, P. D. Kontoyiannis, A. J. Melchiorri, A. G. Mikos, *Tissue Engineering Part C: Methods* **2019**, *25*, 7 411.

[9] Y. M. Hailu, A. Nazir, S.-C. Lin, J.-Y. Jeng, *Materials* **2021**, *14*, 21 6521.

[10] S. Y. Choy, C.-N. Sun, K. F. Leong, J. Wei, *Materials & Design* **2017**, *131* 112.

[11] S. Van Uden, J. Silva-Correia, V. Correlo, J. Oliveira, R. Reis, *Biofabrication* **2015**, *7*, 1 015008.

[12] B. R. Whatley, J. Kuo, C. Shuai, B. J. Damon, X. Wen, *Biofabrication* **2011**, *3*, 1 015004.

[13] D. Wu, J. Tan, L. Yao, J. Tian, B. Luo, L. Li, C. Zhou, L. Lu, *Composites Part A: Applied Science and Manufacturing* **2021**, *147* 106468.

[14] M. Zhu, J. Tan, L. Liu, J. Tian, L. Li, B. Luo, C. Zhou, L. Lu, *Materials Science and Engineering: C* **2021**, *128* 112310.

[15] X. Jin, R. Kang, R. Deng, X. Zhao, Z. Wang, W. Rong, L. Xie, *Journal of Biomaterials Applications* **2022**, *36*, 6 985.

[16] D. H. Rosenzweig, E. Carelli, T. Steffen, P. Jarzem, L. Haglund, *International journal of molecular sciences* **2015**, *16*, 7 15118.

[17] M. M. Panjabi, A. A. White III, *Neurosurgery* **1980**, *7*, 1 76.

[18] M. A. Adams, P. J. Roughley, *Spine* **2006**, *31*, 18 2151.

[19] M. Bhattacharjee, S. Chameettachal, S. Pahwa, A. R. Ray, S. Ghosh, *ACS Applied Materials & Interfaces* **2014**, *6*, 1 183.

[20] R. Borem, A. Madeline, C. Theos, R. Vela Jr, A. Garon, S. Gill, J. Mercuri, *Journal of Biomedical Materials Research Part B: Applied Biomaterials* **2022**, *110*, 5 1056.

[21] C. Correia, S. Bhumiratana, L.-P. Yan, A. L. Oliveira, J. M. Gimble, D. Rockwood, D. L. Kaplan, R. A. Sousa, R. L. Reis, G. Vunjak-Novakovic, *Acta biomaterialia* **2012**, *8*, 7 2483.

[22] D. Hu, D. Wu, L. Huang, Y. Jiao, L. Li, L. Lu, C. Zhou, *Materials Letters* **2018**, *223* 219.

[23] P. P. Raj, *Pain Practice* **2008**, *8*, 1 18.

[24] K. Zolotovsky, S. Varshney, S. Reichert, E. M. Arndt, M. Dao, M. C. Boyce, C. Ortiz, *Communications Materials* **2021**, *2*, 1 35.

[25] G. X. Gu, M. Takaffoli, M. J. Buehler, *Advanced Materials* **2017**, *29*, 28 1700060.

[26] G. X. Gu, F. Libonati, S. D. Wettermark, M. J. Buehler, *Journal of the mechanical behavior of biomedical materials* **2017**, *76* 135.

[27] E. Lin, Y. Li, J. C. Weaver, C. Ortiz, M. C. Boyce, *Journal of Materials Research* **2014**, *29*, 17 1867.

[28] G. D. O'Connell, H. L. Guerin, D. M. Elliott, *Journal of Biomechanical Engineering* **2009**, *131*, 11.

[29] I. M. Shapiro, M. V. Risbud, *2 The Intervertebral Disc: Overview of Disc Mechanics*, Springer, **2014**.

[30] Standard test method for compressive properties of rigid plastics, URL https://www.astm.org/d0695-02.html.

[31] S. L. Stratasys Direct, Inc., Digital materials data sheet, **2018**, URL https://www.stratasys.com/siteassets/materials/materials-catalog/polyjet-materials/
digital-abs-plus/mss_pj_digitalmaterialsdatasheet_0617a.pdf.

[32] Standard test method for tensile properties of plastics, URL https://www.astm.org/d0638-14.html.

[33] S. D. Papka, S. Kyriakides, *Journal of the Mechanics and Physics of Solids* **1994**, *42*, 10 1499.

[34] S. C. Chan, S. J. Ferguson, B. Gantenbein-Ritter, *European spine journal* **2011**, *20*, 11 1796.

[35] N. Newell, J. P. Little, A. Christou, M. A. Adams, C. Adam, S. Masouros, *Journal of the mechanical behavior of biomedical materials* **2017**, *69* 420.

[36] N. Cao, X. Chen, D. Schreyer, *International Scholarly Research Notices* **2012**, *2012*.

[37] M. Sarker, M. Izadifar, D. Schreyer, X. Chen, *Journal of Biomaterials science, Polymer edition* **2018**, *29*, 10 1126.

[38] G. R. López-Marcial, A. Y. Zeng, C. Osuna, J. Dennis, J. M. García, G. D. O'Connell, *ACS Biomaterials Science & Engineering* **2018**, *4*, 10 3610.